Stress-tailoring magnetic anisotropy of V_2O_3/Ni bilayers

Christian T. Wolowiec,[1,*] Juan Gabriel Ramírez,[2] Min-Han Lee,[1,3,†] Nareg Ghazikhanian,[1,3] Nicolas M. Vargas,[1,‡] Ali C. Basaran,[1] Pavel Salev,[1] and Ivan K. Schuller[1]

[1]*Department of Physics, University of California, San Diego, La Jolla, California 92093, USA*

[2]*Department of Physics, Universidad de los Andes, Bogotá 111711, Colombia*

[3]*Materials Science and Engineering Program, University of California, San Diego, La Jolla, California 92093, USA*

(Received 23 December 2021; revised 10 April 2022; accepted 18 May 2022; published 16 June 2022)

We report on a temperature-driven reversible change of the in-plane magnetic anisotropy of V_2O_3/Ni bilayers. This is caused by the rhombohedral to monoclinic structural phase transition of V_2O_3 at $T_C = 160$ K. The in-plane magnetic anisotropy is uniaxial above T_C, but as the bilayer is cooled through the structural phase transition, a secondary magnetic easy axis emerges. Ferromagnetic resonance measurements show that this change in magnetic anisotropy is reversible with temperature. We identify two structural properties of the V_2O_3/Ni bilayers affecting the in-plane magnetic anisotropy: (1) a growth-induced uniaxial magnetic anisotropy associated with steplike terraces in the bilayer microstructure and (2) a low-temperature strain-induced biaxial anisotropy associated with the V_2O_3 structural phase transition. Magnetoresistance measurements corroborate the change in magnetic anisotropy across the structural transition and suggest that the negative magnetostriction of Ni leads to the emergence of a strain-induced easy axis. This shows that a temperature-dependent structural transition in V_2O_3 may be used to tune the magnetic anisotropy in an adjacent ferromagnetic thin film.

DOI: 10.1103/PhysRevMaterials.6.064408

I. INTRODUCTION

The magnetic properties of most materials are strongly dependent on lattice strain. This is especially important for the growth and use of multilayer heterostructures in magnetic devices and applications in which the individual layers can be subject to appreciable stress, owing to a number of causes, including lattice mismatch between adjacent layers. Hence, a successful device that is based on a strained heterostructure relies on the ability to control both the morphology and state of strain in an individual layer. A well-known method for inducing an in-plane uniaxial magnetic anisotropy in a ferromagnetic film is to grow the film on a surface with a terraced microstructure, where an in-plane magnetic easy axis (EA) typically emerges in a direction parallel or perpendicular to the terrace boundaries [1,2,2–6]. Strain is another route for modifying the in-plane magnetic anisotropy in a thin ferromagnetic film [7–9]. However, surface morphology and the state of strain are typically introduced during growth with little or no opportunity for postsynthesis modulation of the magnetic properties of the ferromagnetic film. Recent investigations of the epitaxial growth of ferromagnetic Ni thin films on vanadium oxides demonstrate postsynthesis changes (in addition to growth-induced changes) to the magnetic structure in the Ni layer [10–12].

Vanadium sesquioxide (V_2O_3) is well-known for its coinciding electronic, structural, and magnetic transitions during which the high-temperature (HT) rhombohedral, metallic, and paramagnetic (PM) phases undergo transitions to the low-temperature (LT) monoclinic, insulating, and antiferromagnetic (AFM) phases, upon cooling through a transition temperature of $T_C = 160$ K [13–18]. The LT AFM phase is characterized by ferromagnetic exchange between V-V pairs along the c axis in the monoclinic phase, while the adjacent V_2O_3 $(11\bar{2}0)$ planes perpendicular to the a axis exhibit AFM spin orientation [17,19–21]. Reports of AFM fluctuations above T_C in the PM phase suggest the magnetic degree of freedom is driving the transition to the insulating phase [17,22], in which the PM to AFM transition is accompanied by the opening of an energy gap of ∼0.6 eV at the Fermi surface, leading to a large increase in the electrical resistivity upon cooling [20]. The metal to insulator transition (MIT) in bulk V_2O_3 has been investigated as a function of temperature, applied voltage, applied pressure, and chemical doping, where the change in resistivity across the MIT at $T_C = 160$ K can vary as much as seven orders of magnitude [16,23–26].

The physical properties of V_2O_3 thin films are similar to those of bulk V_2O_3 but are sensitive to strain, substrate orientation, and film thickness. Changes in the magnitude of the resistivity across the MIT are somewhat reduced in thin films of V_2O_3, while T_C for V_2O_3 thin films grown on sapphire substrates with different orientations can vary as much as ∼30 K both above and below the value of T_C for bulk V_2O_3 [13,20,27]. Nonetheless, there is evidence suggesting that the MIT is coupled to the structural phase transition (SPT) in thin films of V_2O_3, in which the growth of metallic domains is bounded by the timescale of the SPT [13,28,29].

*Corresponding author: cwolowiec@physics.ucsd.edu

†Present address: Applied Materials, Santa Clara, California 95054, USA.

‡Present address: General Atomics, San Diego, California 92121, USA.

As a result of the structural change, the volume of the V_2O_3 unit cell expands approximately 1.4% upon cooling into the monoclinic phase, during which there is an increase in the *a* lattice parameter from from 2.87 to 2.91 Å [18]. This expansion can produce an in-plane tensile strain in a thin film that is grown adjacent to the V_2O_3 layer. Numerous reports show that the structural changes in V_2O_3 at T_C significantly affect the coercive fields in neighboring ferromagnetic thin films [10–12,30,31]. Owing to its relatively large coefficient of magnetostriction λ_s [32] and its relatively small value of the saturation field [33], ferromagnetic Ni is easily tuned with field or strain, making it well suited as a controllable magnetic layer when grown in proximity to a functional layer such as V_2O_3. Direct observation of the change in the Ni spin alignment across the SPT in V_2O_3 was recently reported in a V_2O_3/Ni bilayer [34]. However, only a general description of a proximity-induced strain has been given as the cause for the magnetic changes in the neighboring ferromagnetic Ni layer. Specifically, there is still no clear understanding of the mechanism responsible for the emergence of a new anisotropy axis in V_2O_3/Ni bilayers across the first-order phase transition in V_2O_3.

Here we track the temperature-dependent changes to the in-plane magnetic anisotropy and magnetotransport in V_2O_3/Ni bilayer films across the V_2O_3 phase transition. By measuring the x-ray diffraction (XRD), the ferromagnetic resonance (FMR), and the anisotropic magnetoresistance (AMR) of two V_2O_3/Ni bilayer samples, we were able to distinguish between two sources of crystallographic strain: (1) a relatively weak strain in the Ni layer associated with a stressed V_2O_3 layer that is caused by a misalignment of the V_2O_3 (012) plane with the sapphire Al_2O_3 (012) substrate during growth and (2) a strong strain in the Ni layer related to the rhombohedral to monoclinic SPT in V_2O_3 upon cooling through T_C.

We present a scenario in which the strain in the ferromagnetic Ni layer is coupled to the terraced microstructure of the V_2O_3 layer grown on sapphire. The V_2O_3/Ni bilayer experiences a particularly strong strain at the terrace boundaries. Hence, the bilayer becomes elastically weak across the terraces such that the in-plane tensile strain in the Ni layer is effectively uniaxial along the terrace boundaries. Due to the inverse magnetostriction effect and the negative magnetostriction coefficient λ_s of Ni [32,35], this in-plane tensile strain that is directed along the terrace boundaries causes a 90° rotation of magnetic domains within the Ni layer. This scenario is consistent with the emergence of a secondary anisotropy axis across the SPT in V_2O_3 as observed in the FMR, in which there is a change from a HT uniaxial magnetic anisotropy (with one EA parallel to the terrace boundaries) to a LT biaxial magnetic anisotropy with the emergence of a secondary EA that is perpendicular to the terrace boundaries.

As a measure of the spin-dependent scattering, the in-plane AMR corroborates the FMR and the reorientation of the magnetic domains in the thin Ni layer. In a sufficiently strong magnetic field, AMR measurements confirm the typical $\cos^2\beta$ dependence observed for the electrical resistance of polycrystalline ferromagnetic thin films, where β is the angle between the applied dc magnetic field H and the electric current I [36]. A comparison of the spin-dependent scattering in strong field with that at the coercive field H_c suggests that the spontaneous orientation of the magnetic domains in the Ni layer align parallel to the terrace boundaries. Analysis of the AMR at temperatures above and below the structural change in V_2O_3 indicates that there is a 90° strain-induced rotation of magnetic domains within the Ni layer that is consistent with the emergence of the secondary EA observed in the LT FMR.

II. EXPERIMENTAL

Two thin-film V_2O_3/Ni bilayers, V_2O_3(100 nm)/Ni(10 nm)/Pt(3 nm) and V_2O_3(100 nm)/Ni(10 nm)/Al(3 nm), were separately grown on *r*-cut (012) sapphire (Al_2O_3) substrates in a high-vacuum sputtering chamber with a base pressure of $\sim 2 \times 10^{-7}$ Torr. The 100-nm V_2O_3 films were deposited by RF magnetron sputtering at 150 W using a homemade V_2O_3 stoichiometric target. During the deposition of V_2O_3, the sapphire substrates were held at ~700 °C in a 7.8 mTorr Ar atmosphere. After quenching the V_2O_3 layers to room temperature and recovering the base pressure, the 10-nm Ni films were deposited onto the V_2O_3 layers by RF magnetron sputtering at 100 W using an elemental Ni target at room temperature in a 4 mTorr Ar atmosphere. The structures of both samples, obtained from room temperature XRD and reciprocal space maps (RSMs) confirm epitaxial single-phase growth of V_2O_3. The geometry of the x-ray measurements is shown in the schematic displayed in Fig. 1. In-plane FMR measurements of the V_2O_3/Ni bilayers were performed upon cooling from 296 to 100 K using a Bruker BioSpin electron PM resonance spectrometer with a cylindrical cavity resonator at a fixed frequency $f = 9.4$ GHz and a variable dc magnetic field H. The sample was mounted on a quartz rod and rotated through the angle ϕ at two-degree intervals within an accuracy of $\Delta\phi = 0.025°$. At each angle $\phi = 0°,2°,4°$, ...,360°, the applied, in-plane dc magnetic field was swept from 9000 to 0 Oe at a rate of 150 Oe/s, where the in-plane angle ϕ is defined as the angle between the in-plane dc magnetic field H and the uniaxial magnetic EA ($\phi = 0°$). To increase the signal to noise ratio, all FMR measurements were performed with the microwave power kept constant at 1 mW, which avoids any appreciable sample heating. (Results of FMR measurements at higher power are shown in Fig. S4 in the Supplemental Material [37].) The resonance field H_R at each angle was determined from a fit of a derivative of a Lorentzian function to the FMR signal, which appears as the differential absorption of microwave power (see Supplemental Material [37]).

In-plane AMR measurements of one V_2O_3/Ni bilayer sample (with a textured Ni(111) layer) were performed upon warming at 100, 150, and 300 K. Annealed Pt wire leads were affixed using a two-part silver epoxy in a standard linear four-wire configuration to the surface of the top Ni layer of the V_2O_3/Ni bilayer sample so that the electric current is directed at a fixed angle of 45° relative to the uniaxial magnetic EA as shown in the schematic displayed in Fig. 1. [See also the inset in Fig. 6(a) below for a schematic of the electrical leads.] The electrical resistance R was measured using a Quantum Design physical property measurement system with the dc magnetic field H applied parallel to the surface of the V_2O_3/Ni bilayer. The angle between the electric current and the direction of the applied magnetic field was varied in ten degree intervals. At

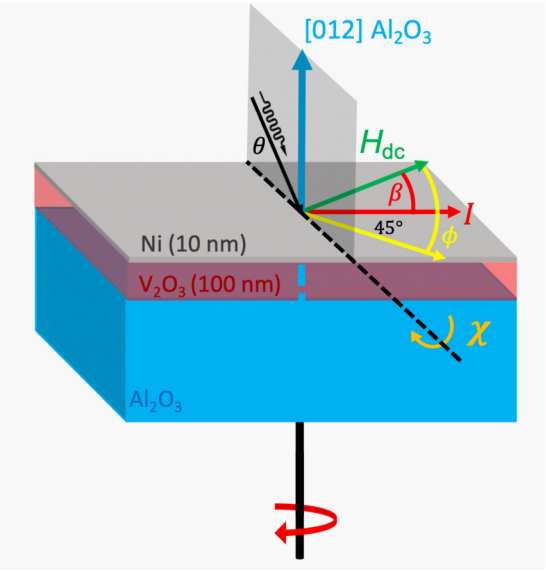

FIG. 1. A diagram of the XRD, FMR, and AMR experiments performed in this investigation. The schematic representation of theV_2O_3/Ni bilayer on an *r*-cut sapphire (Al_2O_3) substrate shows (1) the geometry for the XRD and RSM crystallographic measurements and (2) the in-plane geometry of the FMR and AMR measurements. The x-ray beam is aligned to the Al_2O_3 (012) plane. The angle θ represents the diffraction angle between the beam and the Al_2O_3 (012) plane and the angle χ represents the tilting angle which allows the sample to be rotated before scanning the diffraction angle θ. For the in-plane FMR measurements, the angle between the in-plane dc magnetic field H_{dc} (green arrow) and the magnetic easy axis direction (yellow arrow) is given by ϕ. For the in-plane AMR measurements, the angle between H_{dc} (green arrow) and the electric current I (red arrow) is given by β. (The angle between the electric current I and the easy axis direction is fixed at 45°.)

each angle, the electrical resistance R was measured as the magnitude of H was swept from +1000 Oe to −1000 Oe and then back to +1000 Oe. Due to the orientation of the electric current I relative to the uniaxial magnetic EA, the initial angle of $\beta = 0^\circ$ in the magnetoresistance (MR) measurement corresponds to $\phi = 45^\circ$ in the FMR measurement (see Fig. 1).

III. RESULTS

X-ray measurements were performed on two different V_2O_3/Ni bilayer samples grown on *r*-cut sapphire (Al_2O_3) substrates. XRD and RSMs shown in Fig. 2 confirm the epitaxial growth of a single-phase (rhombohedral) V_2O_3 layer in both samples. The peak at $2\theta \approx 44.2^\circ$ in the XRD pattern of Fig. 2(b) is indicative of a textured face-centered-cubic (fcc) Ni layer with the Ni [111] direction shown in Fig. 2(e) to be nearly parallel to the V_2O_3 [012] direction. The maximum in the intensity in the RSM shown in Fig. 2(d) [indicated by the black dot located at $(\vec{q}_\parallel, \vec{q}_\perp) \approx (1.5\ \text{nm}^{-1}, 30\ \text{nm}^{-1})$] is further evidence of a textured Ni (111) layer in this sample. In contrast, the absence of a Ni peak in the XRD pattern of Fig. 2(a) and the absence of a localized intensity maximum in the RSM shown in Fig. 2(c) together suggest the Ni layer is polycrystalline in this sample.

A comparison of the two RSMs in Fig. 2 shows that while the family of V_2O_3 (012) planes is nearly parallel to the Al_2O_3 substrate in one sample [Fig. 2(c)], the V_2O_3 (012) planes are oblique to the Al_2O_3 substrate in the other sample [Fig. 2(d)]. This is illustrated by the dashed black and red lines drawn in the RSMs of Figs. 2(c) and 2(d). Heavy dashed black lines connect the intensity maxima for the Al_2O_3 (012) and (024) planes, while the heavy dashed red lines connect intensity maxima for the V_2O_3 (012) and (024) planes. The nearly overlapping dashed lines in Fig. 2(c) indicate the family of V_2O_3 (012) and (024) planes are nearly parallel to the substrate. In contrast, the separated dashed lines in Fig. 2(d) indicate the V_2O_3 planes are significantly tilted with respect to the Al_2O_3 (012) plane of the substrate. (Note that there is less of a contrast in the intensity of the V_2O_3 (024) peak in the RSM of Fig. 2(d)). Hence, a plot of the intensity in the vicinity of the V_2O_3 (024) peak in the RSM of Fig. 2(d) is shown in Fig. S1 in the Supplemental Material [37].) A schematic representation of the V_2O_3/Ni bilayer on *r*-cut sapphire (Al_2O_3) substrate shown in Fig. 2(e) illustrates the relative orientation of the V_2O_3 (012) and Al_2O_3 (012) planes. Figure 2(e) can be compared with the geometry of the RSM measurements shown in Fig. 1 in the Experimental section. The real space orientation of the (012) crystallographic planes for V_2O_3 and Al_2O_3 are nearly parallel ($\chi \approx 0.5^\circ$) for the sample with polycrystalline Ni [Fig. 2(c)] but are misaligned at a significant angle of ($\chi \approx 5^\circ$) for the sample with a (111) textured Ni layer [Fig. 2(d)]. For convenience, *pS1* will refer to the V_2O_3/Ni bilayer sample with a polycrystalline Ni layer deposited on a flat V_2O_3 (012) plane, while *tS2* will refer to the sample with a textured Ni layer deposited on an inclined V_2O_3 (012) plane.

In-plane angular-dependent FMR measurements were performed on two V_2O_3/Ni bilayer samples as a function of temperature above and below the V_2O_3 transition at $T_C =$ 160 K. The evolution of the in-plane magnetic anisotropy of sample *pS1* is shown at select temperatures in Fig. 3(a). The solid black curves superimposed on the contour plots represent the angular-dependent resonance field H_R. The value of H_R was determined from a fit of a derivative of a Lorentzian function to the FMR signal at each angle $\phi = 0^\circ$, 2°, 4°, ..., 360°. The angle ϕ is defined as the angle between the applied, in-plane dc magnetic field H and the uniaxial EA (see Fig. 1 in the Experimental section). The interpretation of the FMR results and the use of the derivative of a Lorentzian as a fitting function [39] (shown explicitly in the Supplemental Material [37]) is based on a Landau-Lifshitz-Gilbert (LLG) dynamical model [40,41] for the in-plane magnetization in polycrystalline thin ferromagnetic films with both intrinsic (Gilbert-type) damping and extrinsic in-plane damping related to the terraced microstructure in the V_2O_3/Ni bilayer [42–44]. The HT magnetic anisotropy (at 296 K and 200 K) in the *pS1* sample [Fig. 3(a)] is completely uniaxial with one EA at $\phi = 0^\circ$. The HT magnetic anisotropy in sample *tS2* [Fig. 3(c)] is a superposition of a uniaxial anisotropy (also with an EA at $\phi = 0^\circ$) and a weak biaxial anisotropy with a secondary EA at $\phi = 90^\circ$. (See Figs. S2 and S3 in the Supplemental Material [37] for a complete set of angular-dependent FMR data for both the *pS1* and *tS2* samples at temperatures down to 100 K).

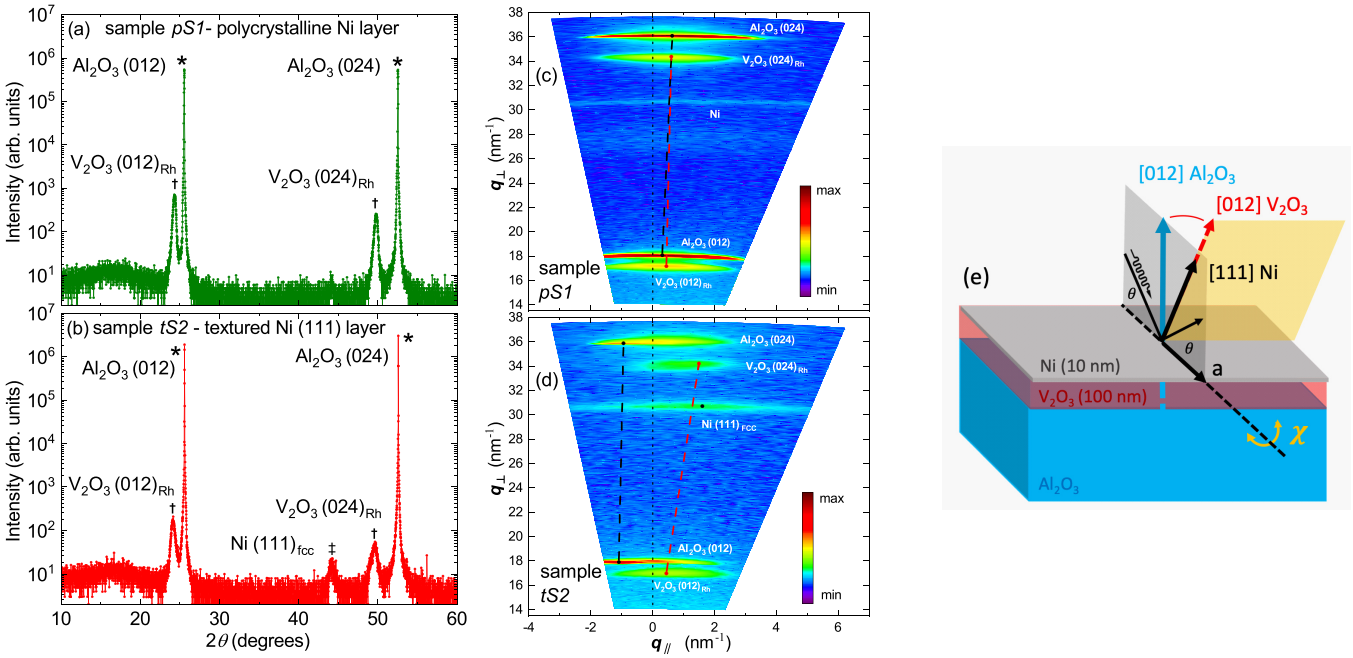

FIG. 2. (a), (b) Room-temperature x-ray diffraction (XRD) for the two different V_2O_3(100 nm)/Ni(10 nm) bilayer samples (a) *pS*1 and (b) *tS*2. The Bragg peaks from the Al_2O_3 (012) and (024) planes are marked by $*$, the V_2O_3 $(012)_{Rh}$ and $(024)_{Rh}$ peaks are marked by † and the Ni (111) peak in panel (b) is marked by ‡. (c), (d) Reciprocal space maps (RSMs) for the two V_2O_3/Ni bilayer samples (c) *pS*1 and (d) *tS*2 with the x-ray beam aligned to the Al_2O_3 (012) plane. (e) Schematic representation of the V_2O_3/Ni bilayer on an *r*-cut sapphire (Al_2O_3) substrate showing the relative orientation of the Ni (111), V_2O_3 $(012)_{Rh}$, and Al_2O_3 (012) planes. The angle θ represents the angle between the beam and the Al_2O_3 (012) plane and the angle χ represents the tilting angle. Variation of χ allows for a rotation of the sample before scanning the diffraction angle θ. The diffraction intensity distribution as a function of θ and χ is recorded in the RSMs shown in panels (c) and (d), which provide information on the relative orientation of the crystal planes in the sample. The in-plane scattering vector is given by $q_\parallel = \frac{2\pi}{\lambda} 2\sin(\frac{\theta\pi}{180})\sin(\frac{\chi\pi}{180})$ and the normal (out-of-plane) scattering vector is given by $q_\perp = \frac{2\pi}{\lambda} 2\sin(\frac{\theta\pi}{180})\cos(\frac{\chi\pi}{180})$, where $\lambda = 1.5406$ Å is the Cu K-α wavelength [38].

Upon cooling, the HT magnetic anisotropy in both samples vanishes near the first-order phase transition in V_2O_3 at 150 K, where phase coexistence leads to an overall magnetically disordered state of the sample. The magnetic anisotropy reemerges in an altered form at LT below the SPT in V_2O_3 [see contour plots at 150 K and 100 K in Figs. 3(a) and 3(c)]. The magnetic anisotropy in both samples at LT exhibits a superposition of a uniaxial magnetic anisotropy (with one EA at $\phi = 0°$) and a biaxial anisotropy (with one EA at $\phi = 0°$ and a secondary EA at $\phi = 90°$). Both samples exhibit a LT biaxial magnetic anisotropy similar to the biaxial anisotropy at HT (296 K and 200 K) observed in the *tS2* sample with a misaligned V_2O_3 layer. This is shown in the angular dependence of H_R for all FMR measurements down to 100 K, summarized in the polar plots shown in Fig. 3(b) for *pS1* and Fig. 3(d) for *tS2*. The elliptically shaped plots of $H_R(\phi)$ shown in Fig. 3(b) indicate a purely uniaxial magnetic anisotropy down to a temperature of 160 K for sample *pS1*. In contrast, the angular dependence of H_R for sample *tS2* at HT exhibits a very weak biaxial character superposed on a predominantly uniaxial magnetic anisotropy [Fig. 3(d)]. Below the V_2O_3 triple transition at $T_C = 160$ K, there is a clear departure in both samples from the predominant uniaxial anisotropy at HT to a biaxial anisotropy at LT.

It is well established that the total magnetic anisotropy energy E_a is determined by the intrinsic magnetocrystalline anisotropy and the extrinsic contributions related to strain (or magnetoelastic anisotropy), shape anisotropy, exchange anisotropy, and the Zeeman energy [45–47]. In the two V_2O_3/Ni bilayer samples investigated here, the magnetoelastic anisotropy is the predominant in-plane contribution. For both the *pS1* and *tS2* samples, the FMR indicates that the in-plane magnetic anisotropy is either uniaxial or a superposition of uniaxial and biaxial anisotropies. Hence, the in-plane magnetic anisotropy energy E_a for the V_2O_3/Ni bilayers in this report can be represented by the following expression [48]:

$$E_a = K_0 + K_U \cos^2(\phi - \phi_1) + K_{ME}\sin^2(2(\phi - \phi_2)). \quad (1)$$

The zero point of the magnetic anisotropy energy is determined by the constant K_0. The second term represents the energy associated with the uniaxial magnetic anisotropy, with a hard axis at an angle $\phi_1 = 90°$ relative to the EA. The third term represents the magnetoelastic energy associated with the biaxial magnetic anisotropy with a hard axis at an angle $\phi_2 = 45°$ relative to the EA [48]. The anisotropy constants K_U and K_{ME} were determined from fits of the resonance field $H_R(\phi)$ to the expression for the magnetic anisotropy energy E_a given in Eq. (1). The determination of K_U and K_{ME} required a conversion of H_R to a magnetic energy density $u_m = BH_R/2$ in units of J/m^3, where $B = \mu_0(H_R + M_S)$ and $M_S = 485$ emu/cm^3 is taken as the saturation magnetization of Ni [33]. Selected fits to H_R at 200 K and 100 K for the *pS1*

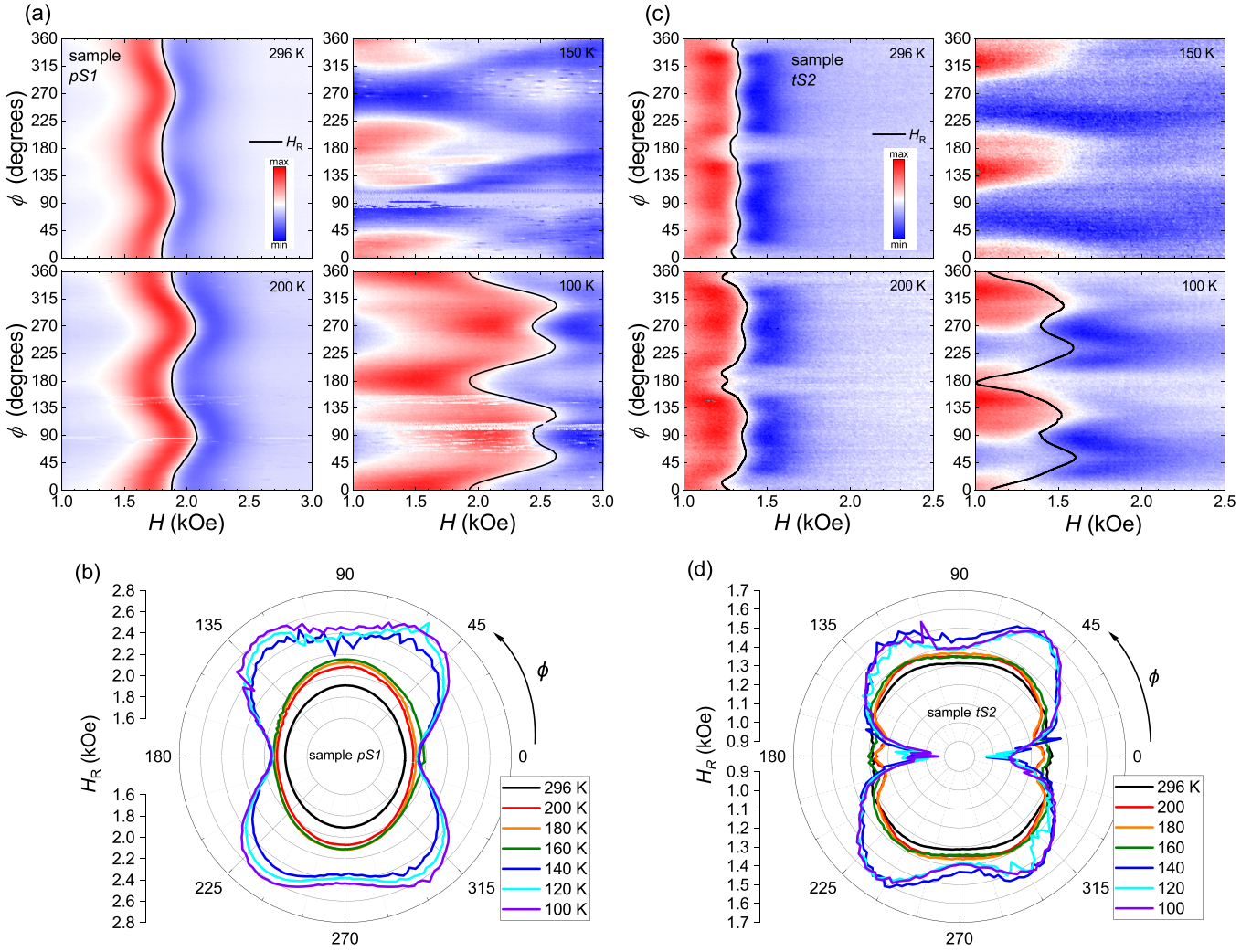

FIG. 3. In-plane angular-dependent ferromagnetic resonance (FMR) measurements of two V_2O_3/Ni bilayer samples. Contour plots of the in-plane FMR signal as a function of dc magnetic field H_{dc} at various temperatures above and below the V_2O_3 SPT for the (a) *pS1* and (c) *tS2* samples. The *y* axis variable ϕ is the angle between H_{dc} and the magnetic easy axis. Blue to red contrast indicates low to high signal intensity. The angular dependence of the resonance field H_R (solid black curve) was extracted from a fit of a Lorentzian derivative function (shown explicitly in the Supplemental Material [37]) to the differential absorption FMR signal. The data shown was taken upon cooling from 296 to 100 K. Warming data (not shown) taken at the same temperatures exhibits nearly identical behavior. (b), (d) Polar representations of the angular dependence of H_R from 296 to 100 K for the (b) *pS1* and (d) *tS2* samples.

and *tS2* samples are shown in Figs. 4(a)–4(d). (See Fig. S5 and Fig. S6 in the Supplemental Material [37] for the complete set of fits at other temperatures.)

The temperature dependence of the anisotropy constants K_U and K_{ME} are plotted in Fig. 5(a). Both anisotropy constants are sensitive to temperature and exhibit significant changes in magnitude upon cooling through the SPT in V_2O_3 at 160 K. In the Ni layer of the *pS1* sample with an unstressed V_2O_3 layer at HT, the magnetic anisotropy is purely uniaxial above the SPT, as indicated by the constant value of K_{ME} near 0 J/m^3 (black squares). (The small positive value for K_{ME} that resulted from the fit is unphysical and reflects the absence of strain in the *pS1* sample.) The sign of K_{ME} for this sample changes from positive to negative at the onset of the induced strain across the SPT in V_2O_3 at 160 K. In contrast, K_{ME} is initially negative at HT in the *tS2* sample (open squares) and exhibits a smaller temperature dependence upon cooling to the SPT at 160 K. The small but nonzero magnitude of K_{ME} at HT in this V_2O_3/Ni bilayer reflects the presence of a slight strain in the Ni layer. Moreover, the slight temperature dependence of K_{ME} down to the SPT as displayed in Fig. 5(a) is also representative of the weak biaxial anisotropy at HT observed in the FMR for this *tS2* sample [see Figs. 3(c) and 3(d)]. The magnitude of K_{ME} jumps significantly for both samples at the onset of the SPT [vertical dashed red line in Fig. 5(a)], indicating a significant proximity-induced strain in the Ni layer at the SPT in V_2O_3. The jump in K_U across the SPT is somewhat weaker for both samples. For the Ni layer of the *pS1* sample (light-blue circles), K_U increases by a factor of 2 to 3 across the SPT from 160 to 140 K. For the Ni layer of the *tS2* sample (open-blue circles), there is hardly any deviation in the extrapolation of the temperature dependence of K_U compared to the jump in K_U across the SPT. This weaker relative change in the uniaxial anisotropy K_U across the SPT is consistent with

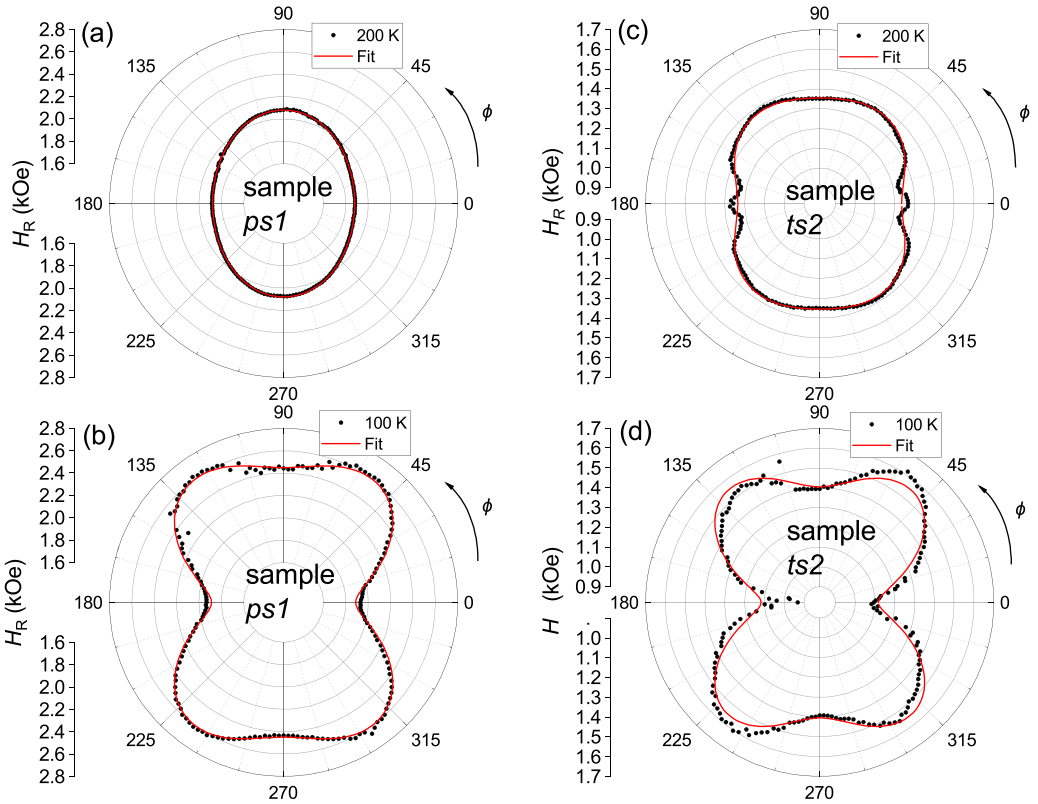

FIG. 4. Representative fits (red curves) of the anisotropy energy E_a [see Eq. (1) in text] to the resonance field lines $H_R(\phi)$ (black circles) for the *pS1* sample at (a) 200 K and (b) 100 K and for the *tS2* sample at (c) 200 K and (d) 100 K. (See Figs. S5 and S6 in the Supplemental Material [37] for the fits at different temperatures.)

the expectation that the microstructure does not change significantly due to strain coming from the SPT in the underlying V_2O_3 layer. The magnitude of K_{ME} can be used to calculate the tensile stress $\sigma_{ts} = \frac{2K_{\mathrm{ME}}}{3\lambda_s}$ [32], where $\lambda_s \approx -34 \times 10^{-6}$ is the negative magnetostriction coefficient for a polycrystalline Ni layer [32]. Figure 5(b) displays the tensile stress σ_{ts} in the Ni layer as a function of temperature. As expected, there is a significant increase in tensile stress σ_{ts} below the SPT at $T_C = 160$ K. The horizontal dashed line at 100 MPa represents the critical stress σ_c at which the magnetoelastic anisotropy becomes comparable to the magnetocrystalline anisotropy in single-crystalline bulk fcc Ni with an anisotropy constant of $K_1 = -5$ kJ/m^3 [45]. This demonstrates that the strain-induced anisotropy associated with the SPT in V_2O_3 is comparable to or can even dominate the intrinsic crystal anisotropy in a textured ferromagnetic thin film.

Measurements of the AMR can be used to detect the strain-induced changes to the magnetization M resulting from in-plane tensile stress [49]. Here, in combination with the FMR measurements, AMR measurements were used to better understand the effect of tensile strain on the magnetic anisotropy in the Ni layer. The AMR measurements were performed on the *tS2* sample upon warming at 100, 150, and 300 K. The magnetic field H was applied parallel to the Ni film surface and the angle between H and the electric current I was varied in intervals of 10°, where the initial angle of 0° corresponds to alignment of the magnetic field H with the electric current I. (See Fig. 1 in the Experimental section and the inset of Fig. 6(a) for a description of the geometry of the AMR measurement. The four-probe configuration shown in the inset of Fig. 6(a) allows for a well-defined direction of electric current I and an easy determination of the angle β between H and I during the AMR measurements.) In this paper, we obtained the MR by measuring the electrical resistance R in a dc magnetic field H applied at a given angle relative to the direction of electric current I. The AMR is the difference between the longitudinal electrical resistance $R_\parallel$ and the transverse electrical resistance $R_\perp$: $\Delta R = R_\parallel - R_\perp$. (Note the longitudinal (transverse) electrical resistance is when the external magnetic field H is applied parallel (perpendicular) to the electrical current.) Figure 6(a) displays the longitudinal and transverse MR curves for the *tS2* sample between $H = -500$ Oe and 500 Oe. At strong magnetic field H, the domains align parallel to H such that $M \| H$. The magnitude of the longitudinal resistance $R_\parallel$ (blue curve for $H_\parallel$) is consistently greater than the transverse resistance $R_\perp$ (black curve for $H_\perp$). This is a characteristic feature of both single crystal and polycrystalline samples of ferromagnetic materials, known as the AMR effect [35,36]. The longitudinal and transverse MR at 100 K and 300 K exhibit the same effect and are included in Fig. S8 of the Supplemental Material [37].

The electrical resistance R is a measure of the spin-dependent scattering of the conduction electrons (s electrons) from the magnetic domains [36,46]. The scattering of the current-carrying s electrons from the localized d electrons is largest (smallest) when the electrons move parallel (perpendicular) to the magnetization M [36,46,50]. This yields the observed difference $R_\parallel > R_\perp$ as displayed in Fig. 6(a). As

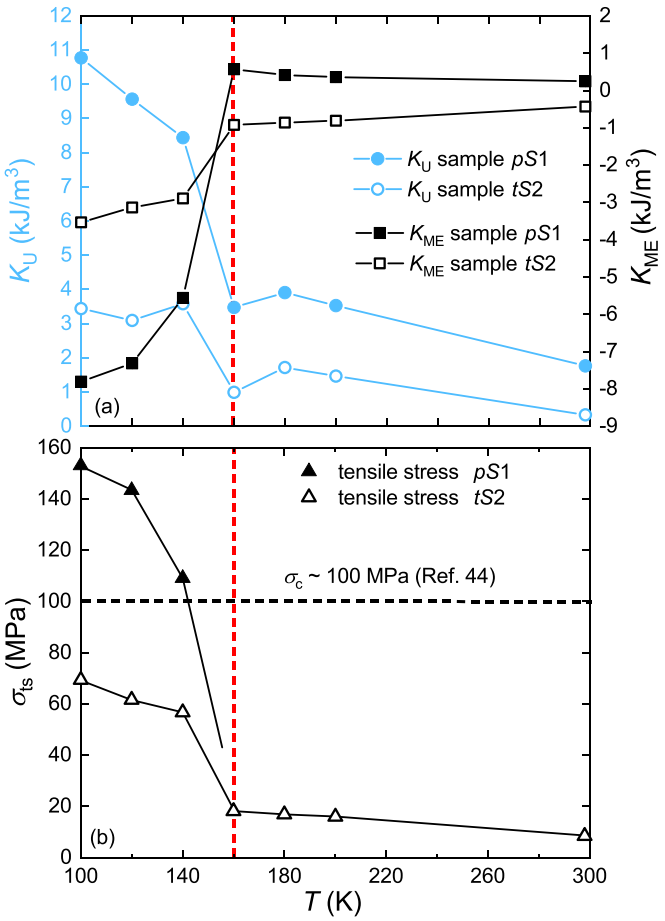

FIG. 5. (a) The temperature dependence of the magnetic anisotropy constants K_U and K_{ME} for the two V_2O_3/Ni bilayer samples *pS1* (filled symbols) and *tS2* (open symbols). The anisotropy constants K_U and K_{ME} were extracted from fits of Eq. (1) to the H_R curves determined from the FMR measurements. The dashed red line marks the V_2O_3 transition temperature T_C. (b) Tensile stress versus temperature (σ_{ts} versus T) for samples *pS1* (solid triangles) and *tS2* (open triangles). The horizontal dashed line indicates the critical stress $\sigma_c = 100$ MPa of ferromagnetic Ni [45]. The extrapolation of σ_{ts} to 0 MPa for sample *pS1* is based on the value of $K_{ME} \approx 0$ kJ/m^3 in panel (a).

the applied magnetic field is reduced from 1000 Oe to 0 Oe in region I and then reversed to a coercive field H_c in region II, the magnetic domains reconfigure so the magnetization M rotates toward the EA along the $\phi = 0°$ direction. At the coercive field H_c, the magnetization M has rotated from its original strong field direction toward the EA and there is a corresponding decrease (or increase) in the MR toward a minimum (or maximum). The values of $R_\parallel$ and $R_\perp$ converge to nearly the same value at the coercive field H_c. This happens at a coercive field of roughly $H_c = \pm 50$ Oe at 300 K, and at $H_c = \pm 170$ Oe at 150 K and $H_c = \pm 190$ Oe at 100 K. Figure 6(b) illustrates the typical $\cos^2\beta$ dependence of the electrical resistance R of a polycrystalline sample of a ferromagnetic material at sufficiently large H. The solid lines are fits of the function $R(\beta) = R_\perp + \Delta R\cos^2\beta$ to the MR data, where $\Delta R = R_\parallel - R_\perp$. This expression for $R(\beta)$ describes the typical angular dependence observed for the electrical resistance in a thin-film

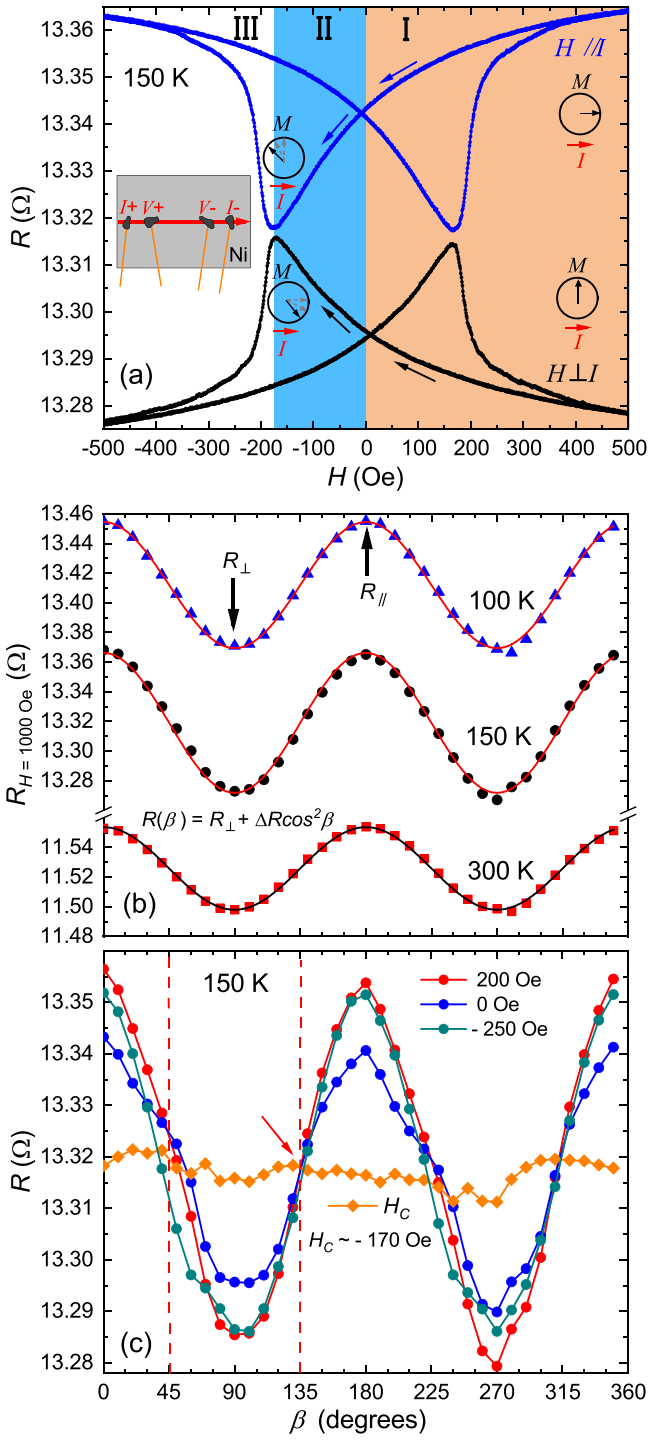

FIG. 6. (a) The longitudinal and transverse magnetoresistance (MR) for the *tS2* sample at 150 K. The blue (black) curves show the MR when the applied magnetic field is parallel $H_\parallel$ (or perpendicular $H_\perp$) to the direction of the electric current I. Inset: A schematic of the four-probe linear configuration of electrical leads affixed to the Ni layer. (b) The angular dependence of the electrical resistance $R(\beta)$ in strong field ($H = 1000$ Oe) at 300, 150, and 100 K. The solid lines are fits of the function $R(\beta) = R_\perp + \Delta R\cos^2\beta$ to the MR data where $\Delta R = R_\parallel - R_\perp$[36]. (c) The angular dependence of the electrical resistance at various field at 150 K. The red arrow indicates there is an equality between R at coercivity H_c and R in a strong magnetic field H when directed at $\beta = 45°$, 135°, 225°, and 315°.

sample of a polycrystalline ferromagnetic material [36]. The angular dependence of the MR at various values of applied magnetic field H, ranging from the saturation field to the coercive field H_c, is shown at 150 K in Fig. 6(c). It is important to emphasize that the $\cos^2\beta$ dependence of $R(\beta)$ vanishes at the coercive field $H_c = -170$ Oe. The magnitude of the electrical resistance $R \approx 13.32\ \Omega$ is nearly constant at H_c and is equal in magnitude to the electrical resistance R when in strong magnetic field H that is directed along $\beta = 45°$, 135°, 225°, and 315°. Similar behavior is observed in the MR for the *tS2* sample above and below the transition temperature T_C, where the values of the electrical resistance at H_c are $R \approx 11.53\ \Omega$ and 13.41 Ω at 300 K and 100 K, respectively. (See Fig. S8 in the Supplemental Material [37].) At these four orientations of the magnetic field ($\beta = 45°$, 135°, 225°, and 315°), the magnetic domains would have angular projections of 45° to the direction of the electric current I. In order for the magnitude of R at the coercive field H_c to be equal to the specific values of $R(45°)$, $R(135°)$, $R(225°)$, and $R(315°)$ in strong field as shown in Fig. 6(c), the scattering mechanism for the itinerant electrons is expected to be similar in each case. This suggests that the domains will align to their default orientation (in a relatively weak field near H_c) that is at a 45° projection relative to the direction of electric current I.

IV. DISCUSSION

A comparison of the structural and magnetic properties of two V_2O_3/Ni bilayer samples at HT and LT allows for an indirect determination of the tensile strain in the Ni layer. Two different sources of strain in the Ni layer are identified. The strongest strain is produced by the SPT from the HT rhombohedral phase to the LT monoclinic phase in V_2O_3 at $T_C = 160$ K. Upon cooling through the SPT into the monoclinic phase, the volume of the unit cell expands approximately 1.4%, during which there is an increase in the a lattice parameter from 2.87 to 2.91 Å [18]. This expansion produces an in-plane tensile strain in the proximal Ni layer. A weaker strain in the Ni layer was observed at HT only in sample *tS2*.

We argue that the HT biaxial anisotropy observed in the FMR for sample *tS2* only [see Fig. 5(c)] is a proximity-induced strain in the Ni layer caused by a distorted rhombohedral phase of V_2O_3. The distortion of the V_2O_3 layer is caused by the misalignment of the V_2O_3 and Al_2O_3 (012) planes and is frozen in at room temperature during growth (see Fig. 2) [13,51]. This distortion in 100 nm films of rhombohedral phase V_2O_3 at room temperature can be comparable in magnitude to the strain produced during the rhombohedral to monoclinic SPT at $T_C = 160$ K [13]. These two different sources of strain (SPT-induced and growth-induced) produce the same biaxial anisotropy, suggesting that the nature of the tensile strain produced in the Ni layer is the same in both cases. The emergence of a strain-induced secondary EA in the magnetic anisotropy serves to identify the direction of tensile strain in the Ni layer. This follows from the negative magnetostriction of ferromagnetic Ni where the strain-induced secondary EA is perpendicular to the direction of tensile strain in the Ni layer [32,35]. Here, we argue that the tensile strain is effectively uniaxial and is directed along the primary EA at $\phi = 0°$, which is parallel to the terrace boundaries in the microstructure of the V_2O_3/Ni bilayer. The growth-induced magnetic EA parallel to the terraces in the microstructure was discussed previously in Ref. [10].

Direct observation of the strain-induced rotation of magnetic domains in Ni across the SPT in V_2O_3 was recently reported in Ref. [34]. First-order reversal curve (FORC) measurements reported in Ref. [10] also indicate that changes to the magnetization of the V_2O_3/Ni bilayer across the SPT in V_2O_3 are caused by irreversible switching mechanisms attributed to an increase in strain-induced pinning [52]. Both the reversible and irreversible domain switching occurs in a magnetostructural landscape, where the individual magnetic domains are confined to the Ni regions bounded by the elongated rips in the microstructure.

Previous reports suggest that the ruptures in the Ni layer occur at the terrace boundaries, where there is a particularly large stress, which sets in initially during film deposition and then subsequently during the V_2O_3 SPT [10,51,53]. This leads to a rupturing of the film where the atomic bonding across the terrace boundary is weaker than the atomic bonding in the material between the terraces. (The flexural strength of Ni, also known as the bend strength or modulus of rupture, can take on values as small as $\sigma_r = 70$ MPa and has a maximum value on the order of $\sigma_r = 935$ MPa [54].) Here, we present a scenario in which the tensile strain is mechanically coupled to the terraced microstructure of the V_2O_3/Ni bilayer. A schematic of the tensile strain in relation to the terrace boundaries is displayed in Fig. 7(a). The ruptures in the film take the form of elongated rips that run parallel to the terrace boundaries as shown in the schematic. As a result, the material in the bilayer is elastically weak in the direction perpendicular to the terraces and cannot sustain components of tensile strain that are perpendicular to the terraces. Hence, the tensile strain (solid brown arrows) is effectively uniaxial and is directed parallel to the terrace boundaries. Figure 7(b) shows an image of the ruptured V_2O_3/Ni film obtained from scanning electron microscopy (SEM). The directionality of the ruptures in theV_2O_3/Ni film is supported by the Fourier transform of the image shown in the inset and is correlated to the direction of the terraces produced by the sapphire substrate (see Ref. [10] containing an atomic force microscopy image of the terraced sapphire substrate). This suggests that the film has reached an elastic limit in the direction perpendicular to the terrace boundaries. The elongated regions of bilayer material located between the terrace boundaries and rips can better sustain the in-plane tensile strain.

The tensile strain competes with the local anisotropy (produced by the terraces, defects, inclusions, grain boundaries, etc.) to produce a secondary EA as observed in the FMR shown in Fig. 3. Owing to the negative magnetostriction coefficient λ_s for Ni, the secondary EA emerges in a direction that is orthogonal to the tensile strain direction, i.e., orthogonal to terrace boundaries [32,35,49]. This multidomain landscape is presented in Fig. 7(c), where the behavior of the individual magnetic domains is governed by the competing influence of an applied magnetic field, the terraces in the microstructure, and the tensile strain. The leftmost schematic in Fig. 7(c) displays the domain configuration (small green arrows) in a sufficiently strong magnetic field H (large green arrow) that is directed at $\beta = 45°$ with respect to the direction of electric

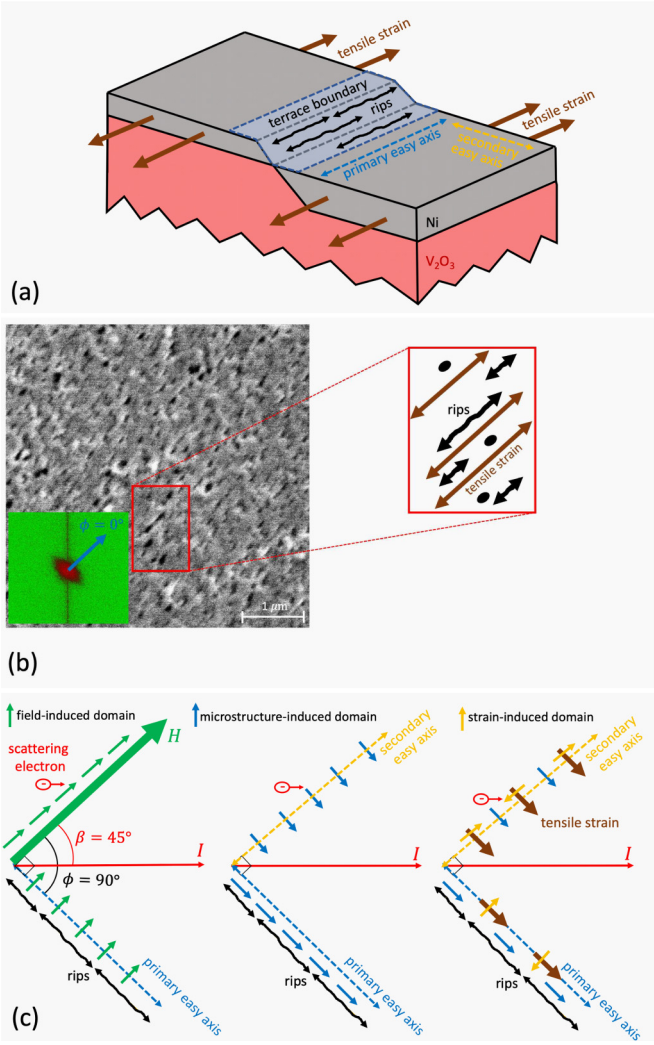

FIG. 7. (a) A schematic (not to scale) of the terraced microstructure of the V_2O_3/Ni bilayer. The tensile strain (brown arrows) is effectively uniaxial along the terraces. The primary easy axis (dashed blue arrow) and strain-induced secondary easy axis (dashed yellow arrow) are parallel and perpendicular to the terrace boundary, respectively. (b) SEM image of the V_2O_3/Ni film on an *r*-cut sapphire substrate (sample *pS*1). The dark concentrated features in the image are rips in the ruptured film. See Fig. S9 in the Supplemental Material [37] for the full SEM image. Inset: Fourier transform of the image showing the microstructure orientation along the primary easy axis (blue arrow) or $\phi = 0°$ in Fig. 3. The tensile strain (brown arrows) exists in regions of material between the elongated rips (black arrows). (c) A schematic of domains at field saturation (green arrows) compared to domains aligned with the terraced microstructure (blue arrows) and strain-induced domains (yellow arrows). The effective scattering angle between conduction electrons (red ovals) and the various domains (green, blue, and yellow) is the same.

current *I*. The spin-dependent scattering occurs with the magnetic domains saturated in an orientation at 45° relative the motion of the itinerant electrons (red ovals). In comparison, the center and right schematic representations in Fig. 7(c) present the default configuration of magnetic domains in a relatively small coercive field H_c. In the absence of tensile strain (center schematic of Fig. 7(c)), the terraces in the surface morphology determine the preferred orientation of magnetic domains (blue arrows), which align parallel to the terrace boundaries [1,3,10]. This spontaneous orientation of domains is reflected in the growth-induced uniaxial magnetic anisotropy that exists at HT and persists through the first-order SPT to lower temperatures. The persistence of the primary EA at $\phi = 0°$ is evident from the temperature dependent FMR shown in Fig. 3. In the presence of a uniaxial tensile strain [right schematic in Fig. 7(c)], the negative magnetostriction λ_s of Ni forces some of the domains (yellow arrows) to rotate perpendicular to the strain direction. This stress anisotropy competes with the local microstructure-induced anisotropy to produce an emergent biaxial anisotropy with a secondary EA at $\phi = 90°$ (see FMR in Fig. 3).

The domain configuration described above suggests an equivalence between the spin-dependent scattering at the coercive field H_c [center and right schematics in Fig. 7(c)] and in strong magnetic field when oriented at $\beta = 45°$ [left schematic in Fig. 7(c)] with respect to the electric current (red arrow).

This is reflected in the AMR, where the constant value of electrical resistance *R* at the coercive field H_c is equal to *R* in a strong magnetic field *H* at $\beta = 45°$, 135°, 225°, and 315°. This is indicated by the red arrows in Fig. 6(c) and in Fig. S8 in the Supplemental Material [37]. Owing to the experimental setup and geometry of the electrical resistance measurement in this study, the direction of the electric current bisects the 90° angle between the primary and secondary magnetic easy axes. (The electric current is fixed at 45° relative to the primary EA at $\phi = 0°$.) This symmetry results in an equivalence between the spin-dependent scattering from domains directed along the primary axis in the absence of strain and the spin-dependent scattering from domains directed along the secondary EA in the presence of strain. Hence, the scattering angle is the same before [Fig. 7(c) center] and after [Fig. 7(c) right] the strain-induced 90° rotation of the magnetic domains. This equivalence in the spin-dependent scattering angle both above and below the SPT supports a scenario for a strain-induced 90° rotation of magnetic domains within the Ni layer that is consistent with the emergence of a secondary EA observed in the FMR.

We note that because the same secondary EA is observed at room temperature in the PM phase above the V_2O_3 phase transition in sample *tS*2, it is unlikely that the pronounced changes in the magnetic structure in the Ni layer are related to the onset of AFM order in the V_2O_3 layer at $T_C = 160$ K. The persistence of an enhanced coercivity across the V_2O_3 phase transition at $T_C = 160$ K, even when the V_2O_3 layer is decoupled from the Ni layer by the insertion of a nonmagnetic Cu spacer layer [12], suggests there is little or no magnetic coupling between the 100 nm V_2O_3 layer and the 10 nm Ni layer. Additional investigations of similar V_2O_3/Ni multilayers also indicate an absence of exchange bias in the V_2O_3/Ni system down to 10 K [55].

V. CONCLUSIONS

We have studied the reversible and controllable changes to the in-plane magnetic anisotropy in V_2O_3/Ni bilayers deposited on *r*-cut sapphire substrates. The magnetic anisotropy

determined from the FMR is described as a superposition of uniaxial and biaxial anisotropy. At HT, the anisotropy is predominantly uniaxial with a single EA. Upon cooling through the structure change in V_2O_3 at 160 K, a secondary strain-induced EA emerges in the Ni. This emergent biaxial anisotropy is caused by the expansion of the lattice during the rhombohedral to monoclinic transition in the underlying V_2O_3 layer. This biaxial anisotropy that emerges upon cooling through the SPT in V_2O_3 is reversible in both V_2O_3/Ni samples studied here. A similar but weaker biaxial anisotropy at HT is observed in one of the V_2O_3/Ni bilayer samples. This biaxial anisotropy is also stress induced, where the tensile strain in the Ni layer is caused by the distortion of the underlying V_2O_3 layer due to misalignment of the V_2O_3 layer with the sapphire substrate. This strain-induced biaxial anisotropy is not reversible and is frozen into the V_2O_3/Ni bilayer during growth.

From the x-ray crystallography, FMR, and AMR, we have indirectly determined the direction of the tensile strain in two V_2O_3/Ni bilayer samples grown on *r*-cut sapphire substrates. Moreover, the tensile strain producing the changes in the magnetic anisotropy is coupled to the terraced microstructure in the V_2O_3/Ni bilayer. Specifically, there is a preferred direction to the rupturing of the Ni layer that is connected to the terrace boundaries. This directionality in the rupturing of the Ni layer forces the in-plane strain in a direction parallel to the terrace boundaries. Hence, the in-plane strain in the Ni layer is effectively a uniaxial strain that is directed along the regions of Ni that exist between the terrace-induced rips. Owing to the negative magnetostriction of Ni, this uniaxial strain along the terrace boundaries accounts for the emergence of a secondary EA that is perpendicular to the primary magnetic EA along terrace boundaries.

We suggest that a reversible and reproducible tensile strain could be used to switch the in-plane magnetic anisotropy in ferromagnetic thin films (in both polycrystalline and quasi-textured layers). This relies initially on the growth-induced uniaxial anisotropy caused by terraces in the microstructure, which overcomes the magnetocrystalline anisotropy as observed in the case of Ni. An additional switchable anisotropy could then be applied externally by the incorporation of the ferromagnetic layer into an active heterostructure. In the V_2O_3/Ni bilayer system investigated here, we take advantage of the structural change in the proximal V_2O_3 layer. In this case, the stress anisotropy produced by the structural transition in the V_2O_3 layer causes an anisotropy comparable or larger than the intrinsic crystalline anisotropy of bulk Ni.

ACKNOWLEDGMENTS

The research was supported by the Department of Energy's, Office of Basic Energy Science, under grant #DE-FG02-87ER45332. J.G.R. acknowledges support from Facultad de Ciencias and Vicerrectoría de Investigaciones of Universidad de los Andes while in STAI at UCSD.

[1] M. Albrecht, T. Furubayashi, M. Przybylski, J. Korecki, and U. Gradman, Magnetic step anisotropies, J. Magn. Magn. Mater. **113**, 207 (1992).

[2] N. Metoki, T. Zeidler, A. Stierle, K. Bröhl, and H. Zabel, Uniaxial magnetic anisotropy of Co films on sapphire, J. Magn. Magn. Mater. **118**, 57 (1993).

[3] D. S. Chuang, C. A. Ballentine, and R. C. O'Handley, Surface and step magnetic anisotropy, Phys. Rev. B **49**, 15084 (1994).

[4] R. K. Kawakami, E. J. Escorcia-Aparicio, and Z. Q. Qiu, Symmetry-Induced Magnetic Anisotropy in Fe Films Grown On Stepped Ag(001), Phys. Rev. Lett. **77**, 2570 (1996).

[5] H.-L. Liu, W. He, Q. Wu, J. Ye, X.-Q. Zhang, H.-T. Yang, and Z.-H. Cheng, Magnetic anisotropy of ultrathin Fe films grown on vicinal Si (111), AIP Adv. **3**, 062101 (2013).

[6] A. V. Davydenko, A. G. Kozlov, and L. A. Chebotkevich, Spatial modulation of in-plane magnetic anisotropy in epitaxial Co(111) films grown on macrostep-bunched Si(111), J. Appl. Phys. **116**, 143901 (2014).

[7] C. Kittel, Physical theory of ferromagnetic domains, Rev. Mod. Phys. **21**, 541 (1949).

[8] E. W. Lee, Magnetostriction and magnetomechanical effects, Rep. Prog. Phys. **18**, 184 (1955).

[9] Y. Liu, B. Wang, Q. Zhan, Z. Tang, H. Yang, Z. Zuo, X. Zhang, Y. Xie, X. Zhu, B. Chen, J. Wang, and R.-W. Li, Positive temperature coefficient of magnetic anisotropy in polyvinylidene fluoride (PVDF)-based magnetic composites, Sci. Rep. **4**, 6615 (2015).

[10] D. A. Gilbert, J. G. Ramírez, T. Saerbeck, J. Tralstoy, I. K. Schuller, K. Liu, and J. de la Venta, Growth-induced in-plane uniaxial anisotropy in V_2O_3 films, Sci. Rep. **7**, 13471 (2017).

[11] J. de la Venta, S. Wang, J. G. Ramirez, and I. K. Schuller, Control of magnetism across metal to insulator transitions, Appl. Phys. Lett. **102**, 122404 (2013).

[12] J. de la Venta, S. Wang, T. Saerbeck, J. G. Ramírez, I. Valmianski, and I. K. Schuller, Coercivity enhancement in V_2O_3/Ni bilayers driven by nanoscale phase coexistence, Appl. Phys. Lett. **104**, 062410 (2014).

[13] Y. Kalcheim, N. Butakov, N. M. Vargas, M.-H. Lee, J. del Valle, J. Trastoy, P. Salev, J. Schuller, and I. K. Schuller, Robust Coupling Between Structural and Electronic Transitions in a Mott Material, Phys. Rev. Lett. **122**, 057601 (2019).

[14] K. Kosuge, The phase diagram and phase transition of the V_2O_3-V_2O_5, system, J. Phys. Chem. Solids **28**, 1613 (1967).

[15] P. D. Dernier and M. Marezio, Crystal structure of the low-temperature antiferromagnetic phase of V_2O_3, Phys. Rev. B **2**, 3771 (1970).

[16] Y. Ueda, K. Kosuge, and S. Kachi, Phase diagram and some physical properties of V_2O_{3+x} ($0 \leqslant x \leqslant 0.080$), J. Solid State Chem. **31**, 171 (1980).

[17] W. Bao, C. Broholm, G. Aeppli, P. Dai, J. M. Honig, and P. Metcalf, Dramatic Switching of Magnetic Exchange in a Classic Transition Metal Oxide: Evidence for Orbital Ordering, Phys. Rev. Lett. **78**, 507 (1997).

[18] A. Singer, J. G. Ramirez, I. Valmianski, D. Cela, N. Hua, R. Kukreja, J. Wingert, O. Kovalchuk, J. M. Glownia, M.

Sikorski, M. Chollet, M. Holt, I. K. Schuller, and O. G. Shpyrko, Nonequilibrium Phase Precursors During a Photoexcited Insulator-to-Metal Transition in V_2O_3, Phys. Rev. Lett. **120**, 207601 (2018).

[19] R. M. Moon, Antiferromagnetism in V_2O3, J. Appl. Phys. **41**, 883 (1970).

[20] B. Sass, C. Tusche, W. Felsch, N. Quaas, A. Weismann, and M. Wenderoth, Structural and electronic properties of epitaxial V_2O_3 thin films, J. Phys.: Condens. Matter **16**, 77 (2004).

[21] D. Grieger and M. Fabrizio, Low-temperature magnetic ordering and structural distortions in vanadium sesquioxide V_2O_3, Phys. Rev. B **92**, 075121 (2015).

[22] J. Trastoy, A. Camjayi, J. del Valle, Y. Kalcheim, J.-P. Crocombette, D. A. Gilbert, J. A. Borchers, J. E. Villegas, D. Ravelosona, M. J. Rozenberg, and I. K. Schuller, Magnetic field frustration of the metal-insulator transition in V_2O_3, Phys. Rev. B **101**, 245109 (2020).

[23] P. Dernier, The crystal structure of V_2O_3 and $(V_{0.962}Cr_{0.038})_2O_3$ near the metal-insulator transition, J. Phys. Chem. Solids **31**, 2569 (1970).

[24] D. B. McWhan, A. Menth, J. P. Remeika, W. F. Brinkman, and T. M. Rice, Metal-insulator transitions in pure and doped V_2O_3, Phys. Rev. B **7**, 1920 (1973).

[25] H. Kuwamoto, J. M. Honig, and J. Appel, Electrical properties of the $(V_{1-x}Cr_x)_2O_3$ system, Phys. Rev. B **22**, 2626 (1980).

[26] S. A. Shivashankar and J. M. Honig, Metal—antiferromagnetic-insulator transition in V_2O_3 alloys, Phys. Rev. B **28**, 5695 (1983).

[27] J. Brockman, N. P. Aetukuri, T. Topuria, M. G. Samant, K. P. Roche, and S. S. P. Parkin, Increased metal-insulator transition temperatures in epitaxial thin films of V_2O_3 prepared in reduced oxygen environments, Appl. Phys. Lett. **98**, 152105 (2011).

[28] E. Abreu, S. Wang, J. G. Ramírez, M. Liu, J. Zhang, K. Geng, I. K. Schuller, and R. D. Averitt, Dynamic conductivity scaling in photoexcited V_2O_3 thin films, Phys. Rev. B **92**, 085130 (2015).

[29] A. Ronchi, P. Homm, M. Menghini, P. Franceschini, F. Maccherozzi, F. Banfi, G. Ferrini, F. Cilento, F. Parmigiani, S. S. Dhesi, M. Fabrizio, J.-P. Locquet, and C. Giannetti, Early-stage dynamics of metallic droplets embedded in the nanotextured Mott insulating phase of V_2O_3, Phys. Rev. B **100**, 075111 (2019).

[30] J. G. Ramírez, J. de la Venta, S. Wang, T. Saerbeck, A. C. Basaran, X. Batlle, and I. K. Schuller, Collective mode splitting in hybrid heterostructures, Phys. Rev. B **93**, 214113 (2016).

[31] T. Saerbeck, J. de la Venta, S. Wang, J. G. Ramírez, M. Erekhinsky, I. Valmianski, and I. K. Schuller, Coupling of magnetism and structural phase transitions by interfacial strain, J. Mater. Res. **29**, 2353 (2014).

[32] B. D. Cullity and C. D. Graham, Magnetostriction and the effects of stress, in *Introduction to Magnetic Materials* (John Wiley & Sons, Ltd., Hoboken, New Jersey, 2008), Chap. 8, pp. 241–273.

[33] C. Tannous and J. Gieraltowski, The Stoner–Wohlfarth model of ferromagnetism, Eur. J. Phys. **29**, 475 (2008).

[34] I. Valmianski, A. F. Rodríguez, J. Rodríguez-Álvarez, M. García del Muro, C. Wolowiec, F. Kronast, J. G. Ramírez, I. K. Schuller, A. Labarta, and X. Batlle, Driving magnetic domains at the nanoscale by interfacial strain-induced proximity, Nanoscale **13**, 4985 (2021).

[35] R. M. Bozorth, Magnetoresistance and domain theory of iron-nickel alloys, Phys. Rev. **70**, 923 (1946).

[36] T. McGuire and R. Potter, Anisotropic magnetoresistance in ferromagnetic 3d alloys, IEEE Trans. Magn. **11**, 1018 (1975).

[37] See Supplemental Material at http://link.aps.org/supplemental/10.1103/PhysRevMaterials.6.064408 for extended data sets and additional details regarding the XRD, FMR, and AMR measurements.

[38] T. Konya, X-ray thin film measurement techniques: III. High resolution X-ray diffractometry, Rigaku J. **25**, 1 (2009).

[39] A. K. Srivastava, M. J. Patni, and B. K. Chaturvedi, Determination of effective linewidth using FMR Line Shape Analysis, J. Phys. IV France **07**, 443 (1997).

[40] L. Landau and E. Lifshitz, 3 - On the theory of the dispersion of magnetic permeability in ferromagnetic bodies, in *Perspectives in Theoretical Physics*, edited by L. Pitaevski (Pergamon, Amsterdam, 1992), pp. 51–65.

[41] T. Gilbert, A phenomenological theory of damping in ferromagnetic materials, IEEE Trans. Magn. **40**, 3443 (2004).

[42] W. Platow, A. N. Anisimov, G. L. Dunifer, M. Farle, and K. Baberschke, Correlations between ferromagnetic-resonance linewidths and sample quality in the study of metallic ultrathin films, Phys. Rev. B **58**, 5611 (1998).

[43] R. Arias and D. L. Mills, Extrinsic contributions to the ferromagnetic resonance response of ultrathin films, Phys. Rev. B **60**, 7395 (1999).

[44] N. G. Chechenin, I. O. Dzhun, G. V. Babaytsev, M. G. Kozin, A. V. Makunin, and I. L. Romashkina, FMR damping in thin films with exchange bias, Magnetochemistry **7**, 70 (2021).

[45] B. D. Cullity and C. D. Graham, Magnetic Anisotropy, in *Introduction to Magnetic Materials* (John Wiley & Sons, Ltd., Hoboken, New Jersey, 2008),Chap. 7, pp. 197–239.

[46] J. M. D. Coey, Ferromagnetism and exchange, in *Magnetism and Magnetic Materials* (Cambridge University Press, New York, 2010), pp. 128–194.

[47] J. M. D. Coey, Micromagnetism, domains and hysteresis, in *Magnetism and Magnetic Materials* (Cambridge University Press, New York, 2010),pp. 231–263.

[48] R. Urban, G. Woltersdorf, and B. Heinrich, Gilbert damping in single and multilayer ultrathin films: Role of interfaces in nonlocal spin dynamics, Phys. Rev. Lett. **87**, 217204 (2001).

[49] R. Asai, S. Ota, T. Namazu, T. Takenobu, T. Koyama, and D. Chiba, Stress-induced large anisotropy field modulation in Ni films deposited on a flexible substrate, J. Appl. Phys. **120**, 083906 (2016).

[50] J. Smit, Magnetoresistance of ferromagnetic metals and alloys at low temperatures, Physica **17**, 612 (1951).

[51] A. S. McLeod, E. van Heumen, J. G. Ramirez, S. Wang, T. Saerbeck, S. Guenon, M. Goldflam, L. Anderegg, P. Kelly, A. Mueller, M. K. Liu, I. K. Schuller, and D. N. Basov, Nanotextured phase coexistence in the correlated insulator V_2O_3, Nat. Phys. **13**, 80 (2017).

[52] J. E. Davies, O. Hellwig, E. E. Fullerton, G. Denbeaux, J. B. Kortright, and K. Liu, Magnetization reversal of CoPt multilayers: Microscopic origin of high-field magnetic irreversibility, Phys. Rev. B **70**, 224434 (2004).

[53] G. Abadias, E. Chason, J. Keckes, M. Sebastiani, G. B. Thompson, E. Barthel, G. L. Doll, C. E. Murray, C. H. Stoessel, and L. Martinu, Review Article: Stress in thin films and coatings: Current status, challenges, and prospects, J. Vacuum Sci. Technol. A **36**, 020801 (2018).

[54] IMMA Handbook of Engineering Materials, 5th ed. (Parkville, Vic.: Institute of Metals and Materials Australasia, Parkville, Victoria, 1997).

[55] M. Erekhinsky, J. de la Venta, and I. K. Schuller, Spin valve effect across the metal-insulator transition in V_2O_3, J. Appl. Phys. **114**, 143901 (2013).